

Solar wind prediction for the Parker Solar Probe orbit

Near-Sun extrapolations derived from an empirical solar wind model based on Helios and OMNI observations

M. S. Venzmer and V. Bothmer

University of Goettingen, Institute for Astrophysics, Friedrich-Hund-Platz 1, 37077 Göttingen, Germany

First draft 9 August 2016; first changes 21 June 2017; received date; accepted date

ABSTRACT

Context. In view of the planned near-Sun spacecraft mission Parker Solar Probe (PSP) (formerly Solar Probe Plus) the solar wind environment for its prime mission duration (2018–2025) and down to its intended closest perihelion (9.86 solar radii) is extrapolated using in situ data. The PSP mission will be humanity’s first in situ exploration of the solar corona. Visiting this yet uncharted region is of special interest, because it will help answer hitherto unresolved questions on the heating of the solar corona and the source and acceleration of the solar wind and solar energetic particles. The solar wind extrapolation of this study is performed within the project CGAUSS (Coronagraphic German And US Solar Probe Survey) which is the German contribution to the PSP mission as part of the Wide field Imager for Solar PRobe (WISPR).

Aims. We present an empirical solar wind model for the inner heliosphere which is derived from Helios and OMNI in situ data. The German-US space probes Helios 1 and Helios 2 flew in the 1970s and observed solar wind in the ecliptic within heliocentric distances of 0.29–0.98 au. The OMNI database at NASA’s Space Physics Data Facility (SPDF) consists of multi-spacecraft intercalibrated in situ data obtained near 1 au. The solar wind model is used together with sunspot number predictions to estimate the frequency distributions of major solar wind parameters PSP will encounter during its mission.

Methods. The model covers the solar wind’s magnetic field strength and its plasma parameters proton density, velocity and temperature. Their individual frequency distributions are represented with lognormal functions. In addition, we also consider the velocity distribution’s bi-componental shape, consisting of a slower and a faster part. The model accounts for solar activity and for solar distance dependency by shifting of these lognormal distributions. We compile functional relations to solar activity by correlating and fitting the frequency distributions with the sunspot number (SSN), using almost five solar cycles of OMNI data. Further, based on the combined data set from both Helios probes, the parameters’ frequency distributions are fitted with respect to solar distance to obtain power law dependencies. Finally, by combining the found solar cycle and solar distance relations, we obtain a simple dynamical solar wind model for the inner heliosphere, confined to the ecliptic region.

Results. The inclusion of SSN predictions and the extrapolation to the PSP perihelion region enables us to estimate the solar wind environment for PSP’s planned trajectory during its prime mission duration 2018–2025. The estimated solar wind values at PSP’s nearest perihelion are: ... Their value vary up to 0.0000 %, arising only from differing amplitude assumptions for the next solar cycle.

Key words. solar wind – sun: heliosphere – sun: corona

1. Introduction

From observations of cometary tail fluctuations Biermann (1951) inferred the presence of a continuous flow of particles from the Sun. With his theoretical solar wind model Parker (1958) formulated the existence of the solar wind even before the first satellites measured it in situ in 1962 (Neugebauer & Snyder 1966).

The idea of a space mission flying through the solar corona dates back to the founding year of NASA in 1958 (ref.). Since then several space missions have measured the solar wind in situ at a wide range of heliocentric distances, in the case of Voyager 1 as far away as 138 au¹, having even left the heliospause into interstellar space (Gurnett et al. 2013). Ulysses was the unique probe that orbited the Sun out of the ecliptic plane and thus could retrieve solar wind measurements from the poles of the Sun (ref.). So far, Helios 2 made the nearest in situ solar wind measurements ever at a distance as close to the Sun as 0.29 au,

closely followed by Helios 1 with 0.31 au (Rosenbauer et al. 1977).

The Parker Solar Probe, with a planned launch date in mid 2018, will reach after six years in 2024 its closest perihelia with 9.86 solar radii, i.e. 0.0459 au. This distance will be achieved through seven Venus gravity assists with orbital periods of 88–168 days. In its prime mission time 2018–2025 PSP provides 24 orbits with perihelia inside 0.25 au (Fox et al. 2015).

The key PSP science objectives are to “trace the flow of energy that heats and accelerates the solar corona and solar wind, determine the structure and dynamics of the plasma and magnetic fields at the sources of the solar wind, and explore mechanisms that accelerate and transport energetic particles” (ref. NASA STDT report, Fox et al. (2015)). To achieve these goals, PSP has four scientific instruments on board: FIELDS for the measurements of magnetic fields and AC/DC electric fields, SWEAP for the measurements of flux of electrons, protons and alphas, ISOIS for the measurement of solar energetic particles and WISPR for the measurement of coronal structures (ref. to

¹ <https://voyager.jpl.nasa.gov/>

each instrument paper).

The Wide field Imager for Solar Probe (WISPR) will contribute to the science goals by deriving the 3D structure of the solar corona through which the in situ measurements are made to determine the sources of the solar wind. It will provide density power spectra over a wide range of structures, e.g., streamers and pseudostreamers, equatorial coronal holes, for determining the roles of turbulence, waves, and pressure-balanced structures in the solar wind. It will also measure the physical properties, such as speed and density jumps, of SEP-producing shocks and their CME drivers as they evolve in the corona and inner heliosphere (Vourlidas et al. 2016).

CGAUSS (Coronagraphic German And US Solar Probe Survey) is the German contribution to the PSP mission as part of the Wide field Imager for Solar PRobe (WISPR). One of the objectives of the CGAUSS project is to extrapolate the solar wind environment down to the closest perihelion of $9.86 R_{\odot}$ distance to the Sun in order to optimize the WISPR and PSP science operations. To achieve that goal this study uses in situ solar wind data from the US-German Helios 1 and 2 space probes and 1 au data from various satellites compiled in the NASA/GSFC OMNI solar wind database.

This paper examines the variations of the bulk solar wind frequency distributions, considers solar activity and extrapolates these distributions to the near-Sun region.

2. Solar wind environment

As a baseline we treat the solar wind primarily as a proton plasma, because the average helium abundance is only about 4.5 % and in slow wind at solar cycle minimum even less than 2 % (Feldman et al. 1978; Schwenn 1983; Kasper et al. 2012). Neglecting heavier ions, the electron and mass density can then be derived accordingly.

The characteristic behavior of a magnetized plasma is determined by its *density*, *temperature* and *magnetic field strength*. Furthermore, the bulk flow *velocity* is the parameter which makes the plasma a 'wind'. For this study we define the solar wind environment through these four major solar wind parameters. Quantities like flux densities, mass flux and plasma beta can directly be derived from those four parameters.

Generally, two types of solar wind are observed in the heliosphere, slow and fast streams (Neugebauer & Snyder 1966), Schwenn (19xx), McComas et al. (19xx)). Fast streams are found to originate from coronal holes as Ulysses polar measurements revealed (ref.). The origin of slow wind is a subject of controversial discussions because several sources are closed magnetic structures in the solar corona, such as Schwenn (19xx) has even reported the possibility of four types of solar wind depending on the phase of the solar cycle/activity.

The solar wind velocity is the defining parameter of the two types of solar wind. Slow solar wind has typical speeds $< 400 \text{ km s}^{-1}$ and fast solar wind has speeds $> 600 \text{ km s}^{-1}$ (see Schwenn 1990, p. 144). Their different compositions and characteristics indicate different sources and generation processes (McGregor et al. 2011b).

Their occurrence frequency varies strongly with solar activity and their interactions lead to phenomena such as stream interaction regions (SIRs) and for quasi-stationary coronal source

regions to co-rotating interaction regions (CIRs, ref. Buch über CIRs).

Embedded in the slow and fast solar wind streams are coronal mass ejections (CMEs) (ref.). Their frequency in near 1 au measurements varies between almost zero during solar cycle minima up to a daily rate of about 0.5 during times of solar maximum (Richardson & Cane 2012).

Since one cannot know which specific solar wind type or structure PSP will encounter at a given point in time during its mission, we extrapolate the parameters' probability distributions from existing solar wind measurements.

Our approach is to get an analytical representation of the frequency distributions' shapes (Sect. 3), their solar activity dependence (Sect. 4) and their solar distance scaling (Sect. 5). We get the parameters' frequency distributions and solar activity dependence from near-Earth solar wind and sunspot number (SSN) time series with a duration of almost five solar cycles and their distance dependency from solar wind measurements of more than half a solar cycle, covering more than two third of the distance to the Sun (0.29–0.98 au).

From the combination of the obtained frequency distributions, SSN dependence functions and solar distance dependence functions we build a general model representing the solar activity and distance behavior of all four solar wind parameter frequencies (Sect. 6).

This general model is then fed with a SSN prediction and extrapolated to PSP's planned orbital positions (Sect. 7).

3. Frequency distributions

This section looks at the solar wind parameters' frequency distributions which we extract from the in situ OMNI data set. We determine adequate fit function types and evaluate how suitable they are to represent the frequencies' shapes.

3.1. OMNI frequency data

The solar wind parameters are highly variable, due to short-term variations from structures like slow and fast wind streams, interaction regions and CMEs, whose rate and properties depend on solar activity. Hence, for deriving general frequency distributions of the solar wind parameters, averaging over long-term solar wind variations is needed. This requires a distance-independent data set covering multiple solar cycles. The abundance of near-Earth hourly OMNI data is well suited for this task, because it spans almost five solar cycles.

This OMNI 2 data set (King & Papitashvili 2005) combines solar wind plasma and magnetic field data and for this study not important energetic proton fluxes, geomagnetic and solar indices. Because it covers decades, the near-Earth solar wind data is composed of intercalibrated multi-spacecraft data which is time-shifted to the nose of the Earth's bow shock.

The data is obtained from the OMNIWeb interface² at NASA's Space Physics Data Facility (SPDF), Goddard Space Flight Center (GSFC). The hourly data of the whole time range up to 2016-12-31 is the basis for the frequency fits. The data starts in 1963-11-27, but the temperature data not before 1965-07-26. The data coverage of the parameters is between 67–74 %, which adds up to about 36–40 years in total. This plethora of data is well suited for our task.

² <http://omniweb.gsfc.nasa.gov/>

We note that the use of higher time resolution instead, would not significantly change our results. The frequency distributions of the also available minutely OMNI data set are almost congruent with the hourly—they only differ slightly at their extreme ends.

We specify bin sizes considering the individual maximal parameter ranges and the OMNI data precision. Especially for the density and temperature we choose their bin sizes such small that their distributions' peaks can be resolved (the peaks are at their lower end). We set the individual bin sizes to 0.5 nT for the magnetic field strength, 10 km s⁻¹ for the velocity, 1 cm⁻³ for the density and 10 000 K for the temperature.

Next, we look for a suitable fit function for the resulting histogram shape of the solar wind parameters' frequency distributions.

3.2. Lognormal fitting

Obviously all possible values for the four parameters are positive. This hints to the supposition that they are lognormally distributed, as many positive natural quantities conform to lognormal distributions. Its probability density function is described by a lognormal function. Therefore we use a lognormal function as the fit function in the process of the least squares regression fitting. The lognormal function

$$W(x) = \frac{1}{\sigma \sqrt{2\pi}x} \exp\left(-\frac{(\ln x - \mu)^2}{2\sigma^2}\right) \quad (1)$$

depends on the location μ and the shape parameter σ . Changes in μ affect both the horizontal and vertical scaling of the function whereas σ influences its shape. The distribution's median x_{med} and mean x_{avg} (average) positions are easier to interpret and can directly be calculated from μ and σ :

$$x_{\text{med}} = \exp(\mu) \iff \mu = \ln(x_{\text{med}}), \quad (2)$$

$$x_{\text{avg}} = \exp\left(\mu + \frac{\sigma^2}{2}\right) \iff \sigma = \sqrt{2 \ln\left(\frac{x_{\text{avg}}}{x_{\text{med}}}\right)}. \quad (3)$$

It is apparent that the mean is always larger than the median. Replacing the variables μ and σ with these relations, the lognormal function (1) becomes

$$W(x) = \frac{1}{2 \sqrt{\pi \ln\left(\frac{x_{\text{avg}}}{x_{\text{med}}}\right)} x} \exp\left(-\frac{\ln^2\left(\frac{x}{x_{\text{med}}}\right)}{4 \ln\left(\frac{x_{\text{avg}}}{x_{\text{med}}}\right)}\right). \quad (4)$$

The values of x_{med} and x_{avg} obtained from fitting the solar wind frequency distributions are listed in Table 1.

From visual inspection, the resulting curves match well with the shape of the magnetic field strength, density and temperature distributions (Fig. 1). However, for the velocity the fit function seems insufficient in describing its more complex shape, especially at its peak position and the faster end of the distribution. Its sum of absolute residuals (SAR) between data and fit is almost three times larger than those from the other parameters (Table 1). They can be compared, because the area of probability density functions is unity.

To reach a better fit result for the velocity we change the fit function. We do not want to abandon the well-founded application of the lognormal function. However, it is reasonable to assume that the velocity distribution can be made up of at least two overlapping branches (McGregor et al. 2011a). Therefore a compositional approach promises better fit results, which is why

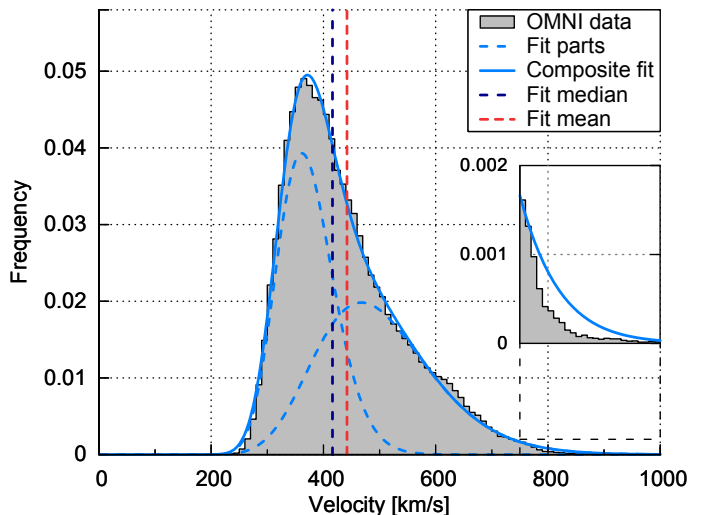


Fig. 2. The velocity's frequency distribution (same as in Fig. 1) and its compositional lognormal fit. The fit's median and mean values and its two fit parts are indicated as well. The inset only has a zoomed-in frequency axis, its x-axis stays the same.

we combine two lognormal functions (4), bearing the disadvantage of more fit variables:

$$W_{\text{II}}(x) = c \cdot W_1(x) + (1 - c) \cdot W_2(x). \quad (5)$$

The balancing parameter c ensures that the resulting function remains normalized as it represents a probability distribution.

The fitting of $W_{\text{II}}(x)$ to the velocity's frequency distribution gives the values of the now five fit parameters (c , $x_{\text{med},1}$, $x_{\text{avg},1}$, $x_{\text{med},2}$ and $x_{\text{avg},2}$), which are also listed in Table 1 together with the median and mean of the composed distribution, which can be derived via solving

$$\int W_{\text{II}}(x) dx = 0 \quad \text{and} \quad \int x W_{\text{II}}(x) dx = 0 \quad (6)$$

respectively.

As anticipated, this more complex fit function is more accurate in describing the velocity's frequency distribution (see Fig. 2). For this reason we keep using the double lognormal ansatz for the velocity frequency fits in the following sections.

In this static model the slow and fast part contribute almost equally ($c \approx 0.5$), which of course is only valid for this kind of long-term average. At different times in a solar cycle their contributions vary strongly.

For the bulk of the solar wind these static lognormal functions describe the parameters' distributions well. This is different for the extreme values (which may also stem from CMEs). The simple lognormal fit models of the magnetic field strength, the velocity and the density underestimate their frequency at the high value tails, whereas the temperature's tail is overestimated (see insets of Fig. 1). The velocity's compositional lognormal fit only slightly overestimates its tail (inset in Fig. 2).

Short-term variations in the solar wind cannot be predicted, but their occurrence rate can. It depends on solar activity, which changes cyclically and thus can be forecasted to a certain degree—at least within a solar cycle.

4. Solar activity variations

This section aims to relate changes in the four solar wind parameters to general solar activity. For this we examine their correlations to the yearly sunspot number and determine the lag times

Table 1. Resulting fit coefficients from the fitting of the lognormal function (4) to the shape of the solar wind parameters' frequency distributions at 1 au (OMNI hourly data). For the velocity also the fit parameters from the double lognormal function (5) are given, as well as the median and mean values of the resulting velocity fit. The mean absolute errors and sums of absolute residuals are shown as well. The values in brackets are the estimated standard deviation of each fit parameter.

Parameter	Median ^a	Mean ^a	Balance	MAE	SAR [%]
	x_{med}	x_{avg}	c		
Magnetic field	5.661(16)	6.164(18)	–	5.51×10^{-4}	6.83
Velocity	4.085(19)	4.183(20)	–	1.80×10^{-3}	18.69
Density	5.276(24)	6.484(34)	–	5.49×10^{-4}	6.48
Temperature	7.470(17)	11.301(32)	–	8.71×10^{-5}	5.78
Velocity	W_1 4.89(14)	5.00(14)	0.504(62)	–	–
	W_2 3.68(20)	3.72(20)	–	–	–
	W_{II} 4.16(14) ^b	4.42(14) ^b	–	3.98×10^{-4}	4.20

Notes. ^(a) Values in their respective units nT, 10^2 km s^{-1} , cm^{-3} and 10^4 K . ^(b) Error estimates derived from the individual fit part errors.

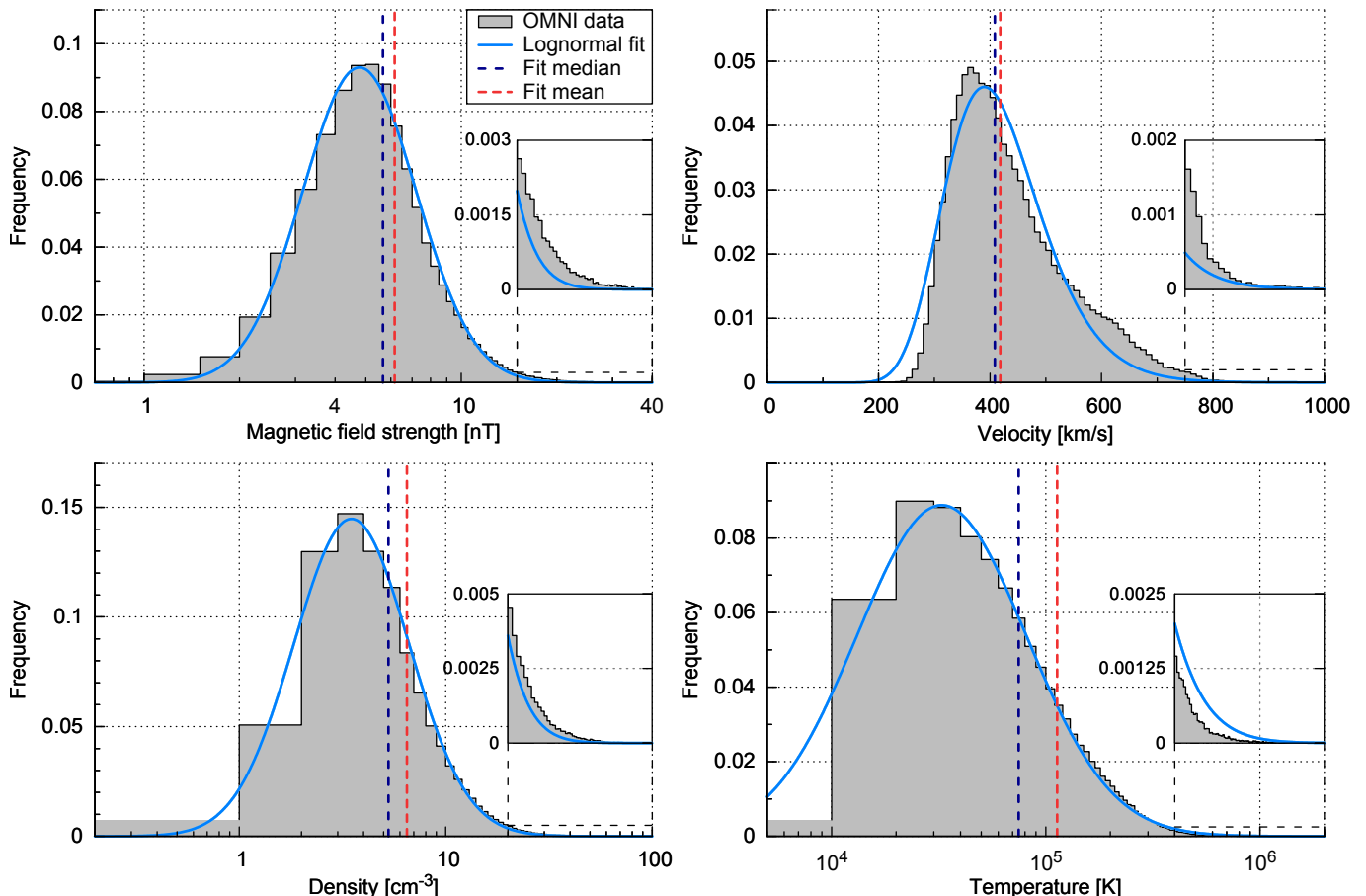


Fig. 1. Frequency distributions of the four solar wind parameters and their lognormal fits. The histograms have bins of 0.5 nT, 10 km/s, 1 cm^{-3} and 10 000 K and are based on the hourly OMNI data set. The fit's median and mean values are indicated as well. The insets only have zoomed-in frequency axes, their x-axes stay the same.

with the highest coefficients. Next, we fit lognormal functions to the frequency distributions like before, but implement linear relations to the yearly SSN to shift the distributions. Only for the velocity the approach is different in that its two components are kept fixed and instead their balance is modified with changing SSN.

4.1. SSN data

Solar activity is commonly measured via the sunspot number. We want to correlate OMNI in situ measurements with the SSN,

yet OMNI data are from Earth orbit, causing variations in solar latitude and distance. To dodge these seasonal variations we use yearly OMNI and SSN data.

The international sunspot number (1963–2016) is retrieved from the online catalogue³ at the World Data Center – Sunspot Index and Long-term Solar Observations (WDC-SILSO), Solar Influences Data Analysis Center (SIDC), Royal Observatory of Belgium (ROB).

³ <http://www.sidc.be/silso/>

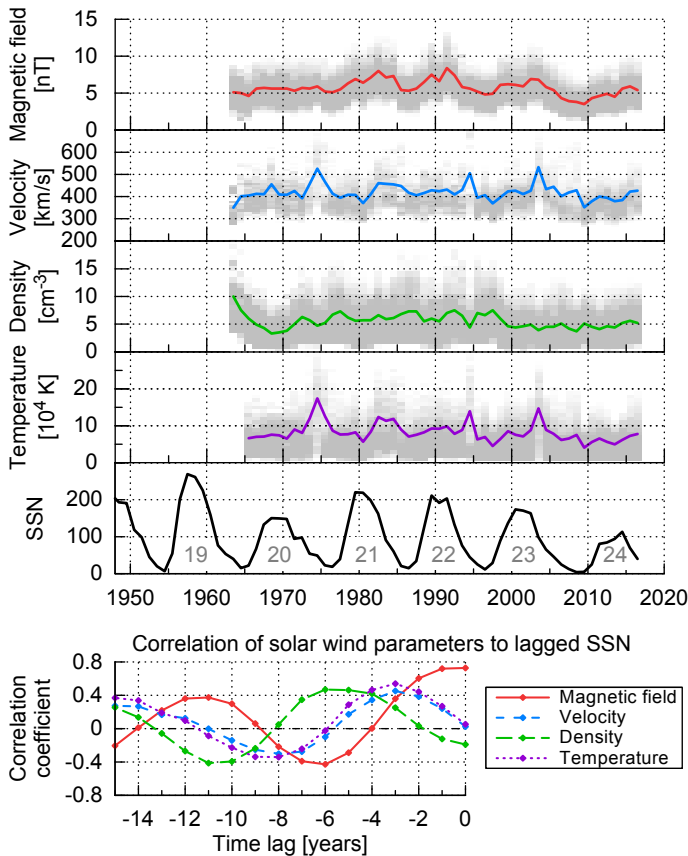


Fig. 3. The solar wind parameter yearly medians from OMNI data and the yearly SSN from the SILSO World Data Center (1963–2016) with cycle number (top). Their correlation coefficients with the yearly SSN are calculated for time lags back to -15 years (bottom).

4.2. SSN correlation

Our current interest lies in the correlation of the SSN to the solar wind median values, because the median defines the position of a lognormal function. The yearly OMNI parameter medians and the yearly SSN are plotted in Fig. 3.

The solar wind velocity and its close friends density and temperature are known to depend on the state of the solar cycle (Schwenn 1983), which is why they follow the SSN indirectly (with time lag). Thus we derive the correlation coefficients for different time lags between solar wind parameters and SSN (see Fig. 3).

The highest correlation coefficient for the magnetic field strength is 0.728, which is without lag time and the highest of all solar wind parameters. This is anticipated because the SSN is directly proportional to the magnetic flux (Smith & Balogh 2003).

Velocity and temperature have a lag time of 3 years with their maximal correlation coefficients (0.453 and 0.540). The density has a lag time of 6 years (0.468), which is in agreement with the by Bougeret et al. (1984) documented density anticorrelation with SSN.

As expected, the correlation coefficients' amplitudes of all parameters decline with increasing lag time and show a frequency of about 11 years.

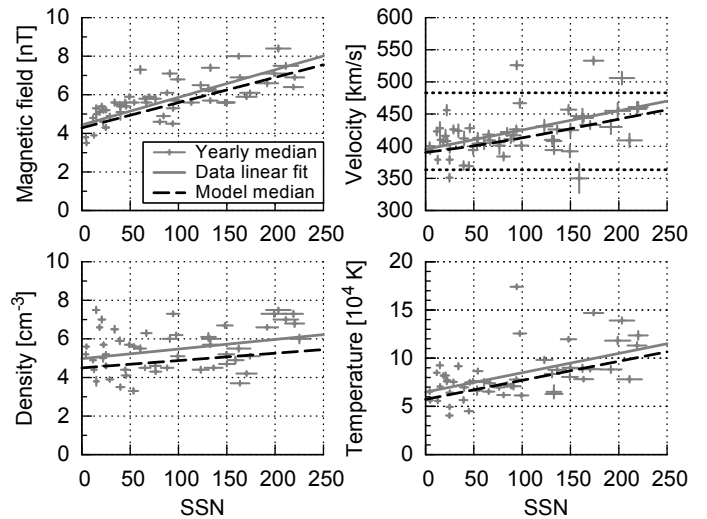


Fig. 5. Solar wind parameter median over lagged SSN. The yearly data medians (+) with their weighted linear fit (solid) are obtained from OMNI data. The error bars denote the SSN standard deviation and the relative weight from the yearly data coverage. The SSN dependent median (7) is from the lognormal model fit (dashed). For the velocity the median is derived from the SSN weighting of the slow and fast model parts, whose magnitudes are SSN independent (dotted).

4.3. SSN fitting

To be able to shift the frequency distributions with SSN, we add a linear SSN dependency to the median

$$x_{\text{med}}(ssn) = a_{\text{med}} \cdot ssn + b_{\text{med}}, \quad (7)$$

using a factor to the SSN a_{med} with a baseline b_{med} . We relate the mean with a scaling factor to the median to transfer its SSN dependency:

$$x_{\text{avg}}(ssn) = (1 + a_{\text{avg}}) \cdot x_{\text{med}}(ssn). \quad (8)$$

With the implementation of these relations into the lognormal function (4), the new dynamic fit function $W'(x, ssn)$ is then fitted to the yearly data. The three resulting fit coefficients (a_{med} , b_{med} and a_{avg}) are presented in Table 2.

Naturally, the fit models match with the general data trends, though single year variations are not able to be replicated by the model (e.g. the high velocity and temperature values in 1974, 1994 and 2003) (see Fig. 4). The comparison with the yearly data median values over SSN shows that the from the model obtained medians have a quite similar slope (see Fig. 5).

Again, the velocity gets a special treatment with the double lognormal distribution (5). It is known that slow and fast solar wind stream occurrence rates follow the solar cycle, yet their magnitudes stay fairly stable (cite?). Thus we keep the two velocity components' positions constant and vary instead their balance with the SSN:

$$c(ssn) = c_a \cdot ssn + c_b. \quad (9)$$

The fit result (see Table 2) is a model in which three years after solar cycle minimum (SSN of zero) the slow solar wind has a share of almost two-thirds and decreases further with increasing SSN (see Fig. 6).

To compare the ratios of slow to fast wind between model and data, we simply apply the commonly used constant velocity threshold of $v_{\text{th}} = 400 \text{ km s}^{-1}$ (cite?). The linear fit to the yearly data ratio and the derived model ratio are quite similar

Table 2. Resulting fit coefficients from the OMNI data fitting with lagged SSN. For the velocity the fit parameters from the double lognormal fit and their balancing function are given. The values in brackets are the estimated standard deviation of each fit parameter.

Parameter	Median ^a		Mean ^a	Balance	
	SSN factor a_{med}	Baseline b_{med}		Scaling factor a_{avg}	SSN factor c_a
Magnetic field	$1.309(19) \times 10^{-2}$	4.285(17)	$8.786(78) \times 10^{-2}$	—	—
Density	$3.81(25) \times 10^{-3}$	4.495(26)	$3.050(27) \times 10^{-1}$	—	—
Temperature	$1.974(26) \times 10^{-2}$	5.729(19)	$6.541(28) \times 10^{-1}$	—	—
Velocity	W'_1 W'_2	— —	3.633(12) 4.831(81)	$1.008(37) \times 10^{-2}$ $2.31(20) \times 10^{-2}$	$-1.799(95) \times 10^{-3}$ 0.638(32)

Notes. ^(a) Values in their respective units nT, 10^2 km s^{-1} , cm^{-3} and 10^4 K .

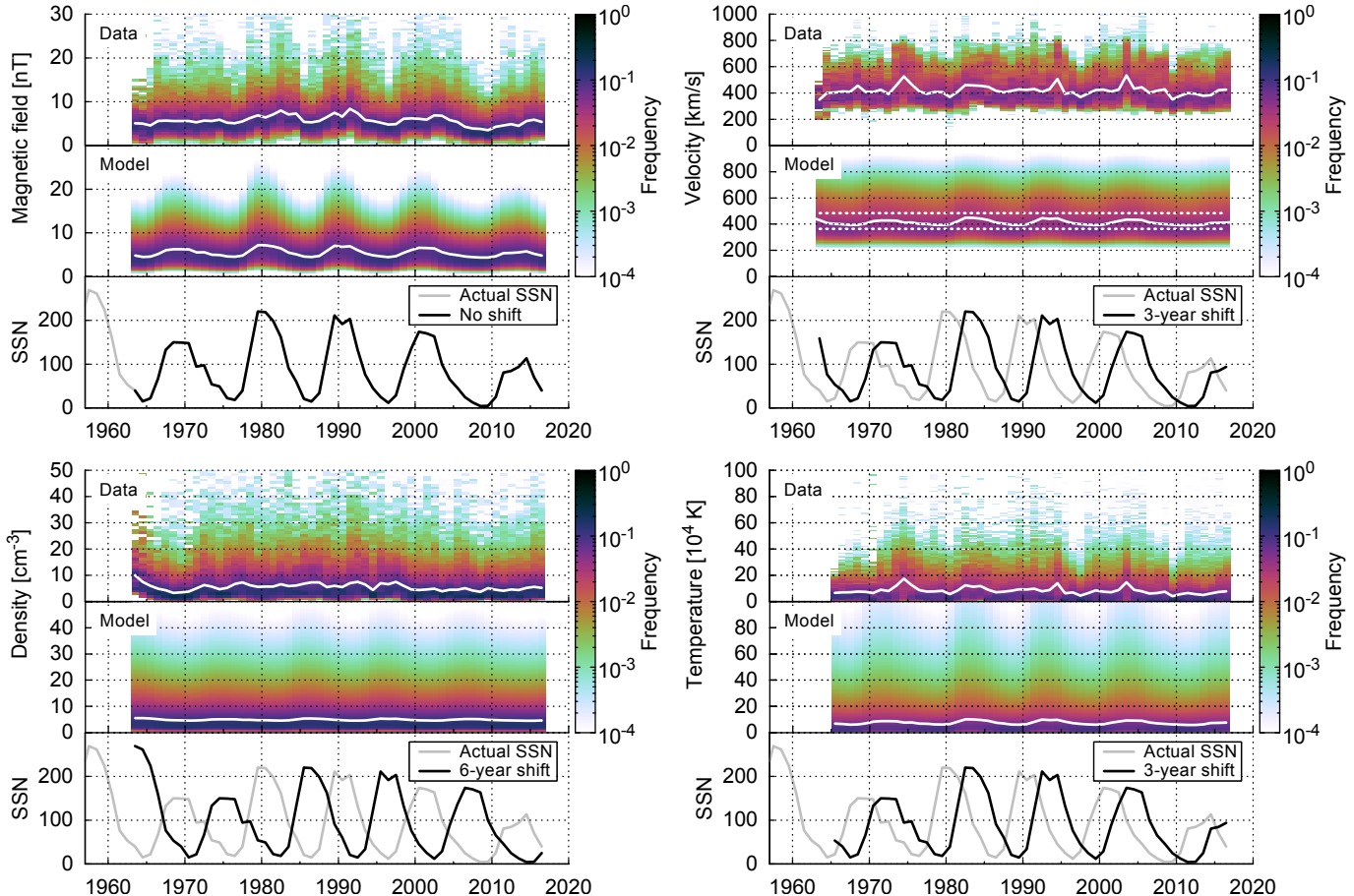


Fig. 4. Solar wind parameter data frequencies, lognormal fit models with their median values (white) and the corresponding yearly SSN (grey) over the OMNI time period 1963–2016. The for the models shifted SSN is indicated by a black line. The velocity median is derived from the SSN weighted constant lognormal parts (dotted).

(see Fig. 6). Specific velocity thresholds between slow and fast solar wind cannot be directly compared with the to some degree steeper balance parameter of this model. The model's balance may represent the actual ratios of the solar wind types in a more realistic way than a specific velocity threshold does, since the velocity ranges of both types overlap (McGregor et al. 2011a).

5. Solar distance dependency

In this section we use Helios data to obtain power law fit functions for the heliocentric distance dependency and also evaluate the fits' extrapolation behavior in direction to the Sun. To fit the bulk solar wind distributions' distance dependency we use the frequency fitting method from Sect. 3 on distance-binned Helios

data. This results in models comprising of with distance shifted lognormal functions.

5.1. Helios distance data

The Helios probes were the only spacecraft measuring in situ solar wind over large solar distance ranges in the inner heliosphere. We use the combined data from both Helios 1 and Helios 2 probes. Helios 1's (Helios 2's) highly elliptical orbit in the ecliptic covered a solar distance range of 0.31–0.98 au (0.29–0.98 au). Launched during solar cycle minimum, the data of both probes cover the rise to the maximum of cycle 21 (~6.5 years at varying distances).

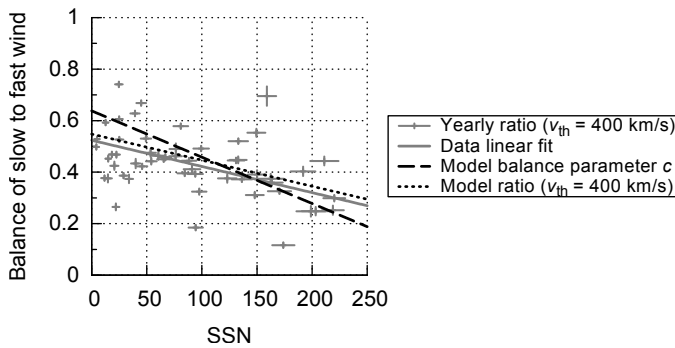


Fig. 6. Balance of slow to fast solar wind over the by 3 years lagged SSN. The yearly ratios (+) and their weighted linear fit (solid) are obtained from OMNI data with a threshold velocity of $v_{\text{th}} = 400 \text{ km s}^{-1}$. The error bars denote the SSN standard deviation and the relative weight from the yearly data coverage. The model's balance parameter (9) and derived ratio (same threshold) are plotted as dashed and dotted lines.

Again we choose data with hourly resolution to allow its use along with the hourly OMNI data. As Schwenn (1983) pointed out, the many hourly Helios data points which contain only a few measurements, contribute with a larger scatter to the frequency distributions, nevertheless their effect is insignificant in the treatment of the bulk data.

Helios 1's (Helios 2's) merged hourly data set from the magnetometer and plasma instruments (Rosenbauer et al. 1977) includes ~ 12.5 orbits (~ 8 orbits) in the time range 1974-12-10 to 1981-06-14 (1976-01-01 to 1980-03-04). The Helios data was retrieved from the Coordinated Data Analysis Web (CDAWeb) interface at NASA's GSFC/SPDF⁴.

The Helios 1 (Helios 2) magnetometer data coverage is about 43 % (54 %) and amounts to 2.8 years (2.3 years) in total. The plasma data coverage is 76 % (92 %) and amounts to 5.0 years (3.9 years) in total. Thus, the Helios data cover only fractions of a solar cycle and cannot be used for deriving representative time-independent solar wind multi-cycle conditions like the OMNI data can.

Using this data, we also have to keep in mind that its time coverage is unequally distributed over the solar cycle. Dividing the data by the transition from cycle minimum to maximum (mid 1977) and considering the data gap distributions, the Helios data covers about 68 % during cycle minimum whereas during maximum only 38 %.

For calculating the median and mean values at different solar distances the data is binned into 0.01 au bins, which is also the native precision in this data set.

5.2. Power law fitting

A power law scaling distance behavior is expected from all four parameters (cites?). Therefore we use the power function

$$x(r) = d r^e \quad (10)$$

with the solar distance r for the regression fit of the median and mean. The fits are weighted by data counts per bin. With r in astronomical units we get the fit coefficients (d_{med} , d_{avg} , e_{med} and e_{avg}) as given in Table 3.

As expected, the velocity exponents match with those from Schwenn (1983, 1990), who derived the distance dependencies for both Helios spacecraft separately ($v_{\text{HI}}(r) \propto r^{0.083}$ and

$v_{\text{H2}}(r) \propto r^{0.036}$). Likewise, the density exponents agree well with the Helios plasma density model, which Bougeret et al. (1984) derived from Helios data and normed to the 1976 1 au density ($n(r) = 6.14 r^{-2.10} \text{ cm}^{-3}$).

The next step is to fit the bulk of the solar wind parameters with lognormal functions. At all considered solar distances the mean of the three plasma parameters is larger than their median (Fig. 7).

The large velocity's crossing distance and its large error indicate that the median's and mean's distance behavior can be kept identical and so the frequency's shape distance independent.

However, the magnetic field strength's mean crosses the median at 0.339 au and is lower at smaller distances (Table 3). At the crossing point and below the magnetic field strength can therefore not be described anymore with a lognormal function. For an extrapolation to the PSP perihelion the same happens for the temperature at 0.082 au.

Those crossings limit the possible extrapolation distances with lognormal functions. To circumvent these limitations for all four solar wind parameters we set the exponents e_{med} and e_{avg} to be identical, avoiding crossing of median and mean. Then the distribution's width has a power law scaling with solar distance. Applying this approximation, we have to accept larger model errors, especially for the magnetic field strength. It also limits the extrapolation accuracy, however it keeps the model simpler.

5.3. Power law lognormal fitting

To retrieve the frequency distributions for every 0.01 au solar distance bin, we choose the same solar wind parameter binning as with the OMNI data (Sect. 3.1).

As mentioned before, we set the exponents of median and average to be identical. Implementing the power law distance dependency (10) into the lognormal function (4), we get three fit parameters (d'_{med} , d'_{avg} and the common exponent e'). Naturally, we use the double lognormal function (5) for the velocity distribution fit, resulting in $W''_{\text{II}}(x, r)$. The additional fit parameters are the balancing parameter c' and from the second lognormal part $d'_{\text{med},2}$ and $d'_{\text{avg},2}$. The resulting fit coefficients for the four solar wind parameters are presented in Table 4.

With $c' = 0.557$ the velocity balancing parameter is of an expected value similar to that obtained from the Helios time period (the mean SSN during the Helios period was 59, this corresponds to $c(59) = 0.53$; see Fig. 6).

The fit models seem to resemble the data quite well (Fig. 8). The magnetic field strength frequency is more focused (around 40 nT) at the lower distance boundary than the model's is. This is expected because of our fixed distance independent shape approximation. The velocity and temperature models' upper values have a higher frequency than the data shows. This is due to the systematic fit discrepancy of the lognormal distribution's high value tails (see zoom box in Fig. 1).

5.4. Distance scaling law variations

relocate section to 5.3?

This radial solar wind model represents the Helios time frame around the rise of solar cycle 21. It is known that the solar wind parameters' magnitudes vary with solar activity. Looking at the variation of the yearly distance scaling laws (Fig. 9), there is no systematic variation for the magnetic field. The exponents

⁴ <http://spdf.gsfc.nasa.gov/>

Table 3. Fit coefficients for the median and mean solar distance dependencies of the four parameters from the combined Helios data set. The errors in brackets are the estimated standard deviations of each fit parameter. The crossing distance is the point where the fitted median and mean intersect. The year variation is the weighted standard deviation from all yearly fitted exponents.

Parameter	Median		Mean		Crossing distance [au]	Year variation Δe
	d_{med}^a	e_{med}	d_{avg}^a	e_{avg}		
Magnetic field	5.377(92)	-1.655(17)	6.05(10)	-1.546(18)	0.339(11)	0.11
Velocity	4.107(28)	0.058(13)	4.356(24)	0.049(10)	$0.7(83) \times 10^3$	0.012
Density	5.61(27)	-2.093(46)	7.57(30)	-2.010(38)	0.027(73)	0.072
Temperature	7.14(23)	-0.913(39)	9.67(21)	-0.792(28)	0.082(85)	0.005

Notes. ^(a) Values in their respective units nT, 10^2 km s^{-1} , cm^{-3} and 10^4 K .

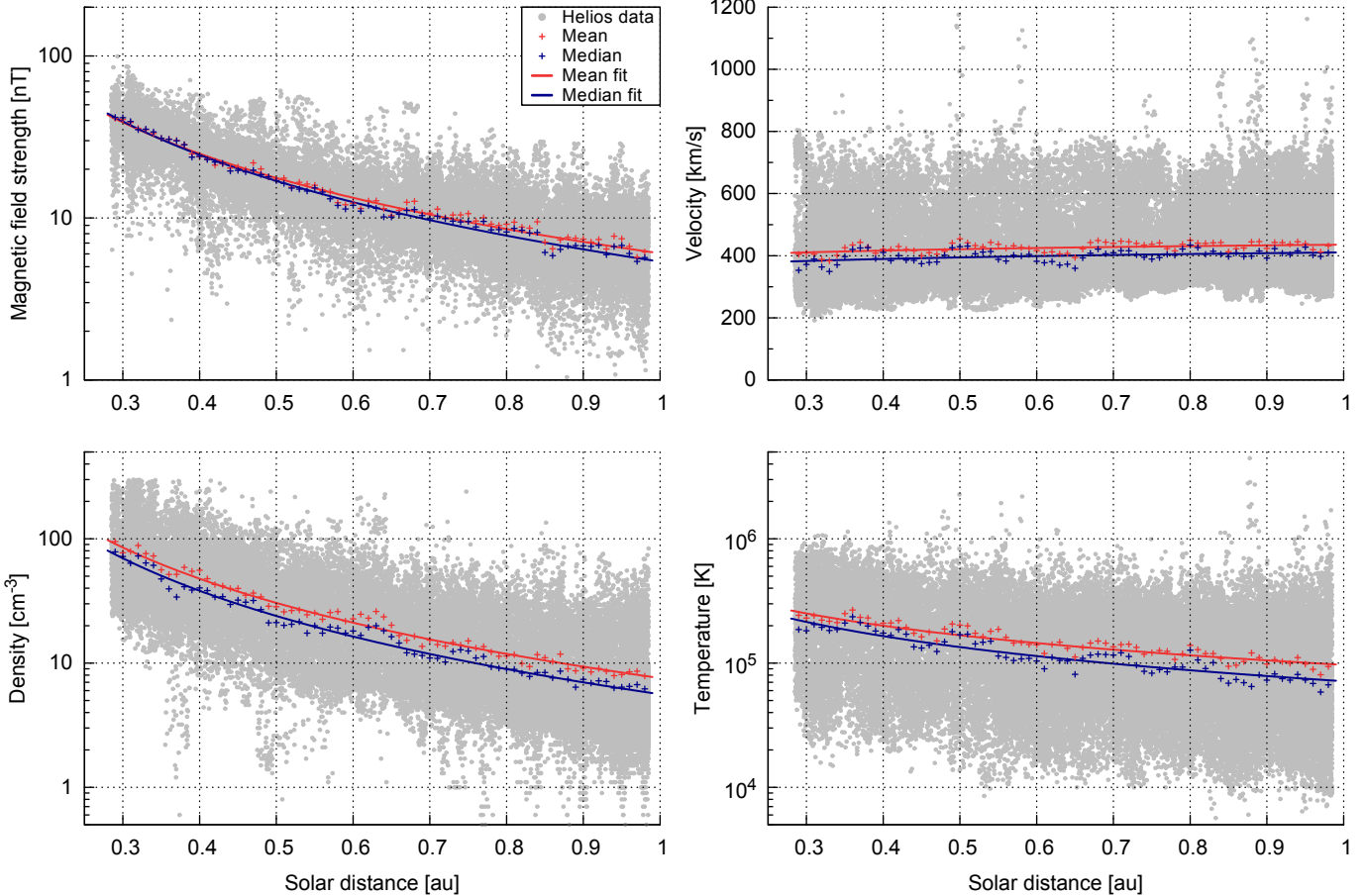


Fig. 7. Helios hourly data plots of the four solar wind parameters over solar distance. The mean and median per 0.01 au data bin and their fit curves are plotted as well. The Helios data has a native distance resolution of 0.01 au. To make the abundance visible in these plots, we added a random distance value of up to ± 0.005 au.

Table 4. Fit coefficients from the single lognormal power function, respectively double lognormal for the velocity (combined Helios data). The errors in brackets are the estimated standard deviations of each fit parameter.

Parameter	Median ^a d'_{med}	Mean ^a d'_{avg}	Exponent e'	Balance c'
Magnetic field	5.358(25)	5.705(28)	-1.662(11)	—
Density	5.424(33)	6.845(47)	-2.114(20)	—
Temperature	6.357(64)	10.72(14)	-1.100(20)	—
Velocity	W''_1 5.26(13)	3.707(13)	3.748(16)	0.0990(51)
	W''_2	5.42(11)		0.557(45)
	W''_{II}	4.13(13) ^b	4.47(11) ^b	—

Notes. ^(a) Values in their respective units nT, 10^2 km s^{-1} , cm^{-3} and 10^4 K . ^(b) Velocity median and mean 1 au values for the resulting function. Error estimates derived from the individual fit part errors.

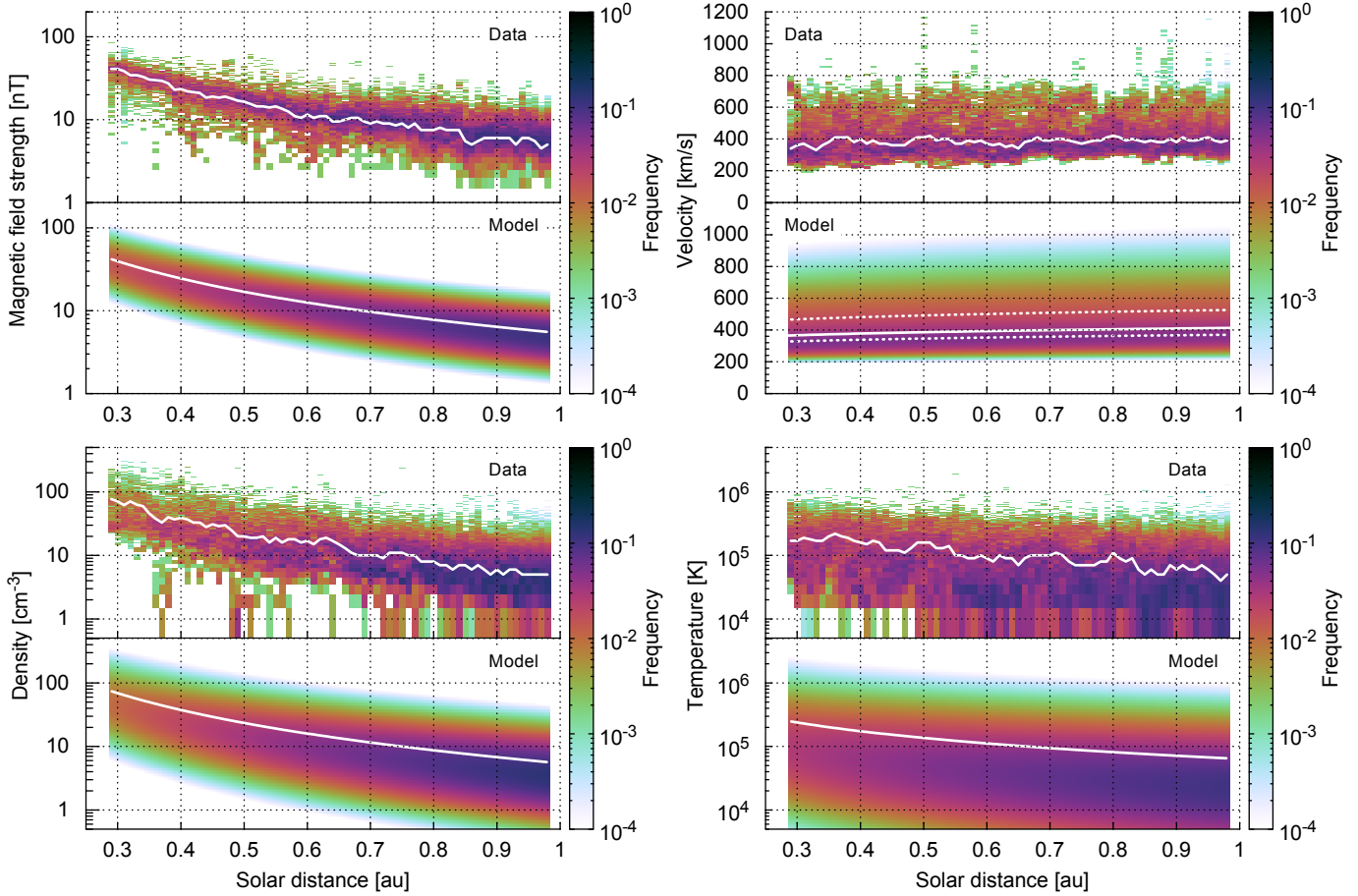


Fig. 8. Solar wind parameter's frequency distributions over solar distance. Plotted are the binned Helios data and the power law lognormal fit model (double lognormal for the velocity) with their median values (white).

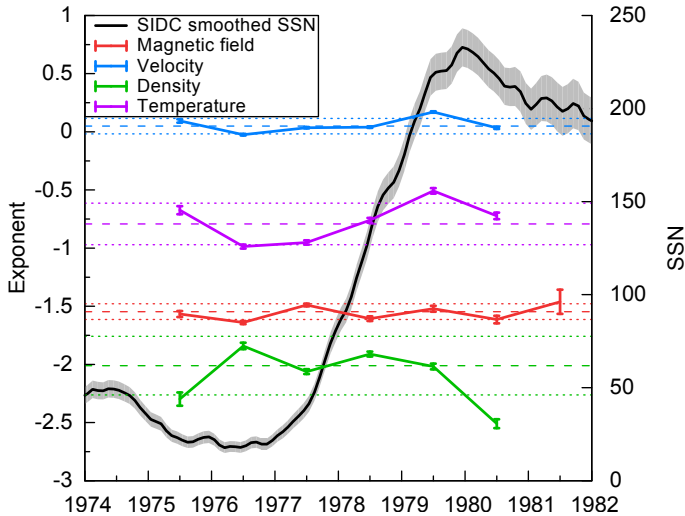


Fig. 9. Helios year variation of the solar wind parameters' fit exponents and SIDC 13-month smoothed monthly SSN. In this plot the year 1974 is omitted because the 21 days covered only

of velocity and temperature seem to follow the SSN and the density not...

For simplicity we assume that the distance scaling laws are time independent and account for this approximation with including the calculated exponents' yearly variations (Table 3)

as uncertainties.

make remark about influence of unequal solar cycle coverage... (sect. 5.1)

Possible differing scaling laws at smaller heliocentric distances are discussed in Sect. 7.

6. General solar wind model

Finally, we combine the obtained solar activity and distance dependencies for shifting the frequency distributions. The result is an empirical solar wind model for the inner heliosphere.

Under the assumption that the fall-off laws do not change with time/solar activity (as shown above...), they can be used in general.

We combine the fit coefficients of the median relation for solar activity dependence (7) with the ones from the power law distance dependence (previous section)

$$x_{\text{med}}(ssn, r) = (a_{\text{med}} \cdot ssn + b_{\text{med}}) \cdot r^{e'} \quad (11)$$

to get the combined model function $W'''(x, ssn, r)$. And for the velocity $W''_I(x, ssn, r)$ with the double lognormal function (5).

empirical model limits (spherical coordinates):

- heliocentric distance range 0.29–0.98 au

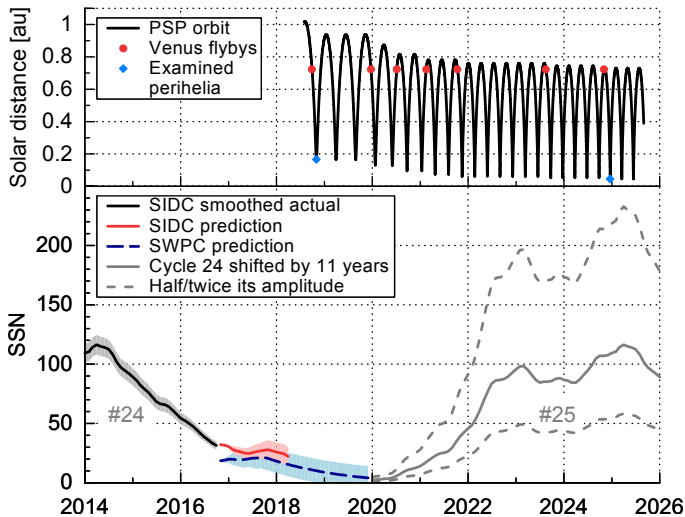


Fig. 10. PSP's solar distance during its mission time (top). Consecutive Venus flybys bring its perihelia nearer to the Sun. Actual and predicted SSN (bottom), i.e. SIDC 13-month smoothed monthly actual SSN, SIDC prediction, SWPC prediction and simply by 11 years shifted SSN from previous cycle 24, together with two alternative trends of half and twice its amplitude.

- rotational symmetry
- confined to ecliptic ($\pm 7.2^\circ$ HGI)
- model constrictions:
- solar distance dependency function
- frequency distribution functions
- neglected influence from heliolatitude variation

7.2. Near-Sun extrapolation for PSP orbit

Parker Solar Probe is planned to launch in mid 2018. With its first Venus flyby it will swing into Venus' orbital plane (3.86° to Sun's equator/ 3.39° to ecliptic), which allows for additional seven flybys to finally reduce its perihelion distance to a minimum of less than $10 R_s$ (Fox et al. 2015) (Fig. 10).

For the extrapolation to PSP's orbital range we just assume that our derived distance scaling laws do not change. The comparison with existing near-Sun models reveals that this is not entirely true (Fig. 11).

The magnetic field magnitude from our extrapolation is flatter than the analytical magnetic field model from Banaszkiewicz et al. (1998), who constructed a dipole plus quadrupole plus current sheet (DQCS) model. We attribute this effect to the from a lognormal shape deviating distribution (see Sect. 5.2).

Alfvénic critical surface i.e. source surface (see Fox before 2.1)

in direction to the Sun is at about $2.5 R_s$ the source surface (Schatten1969)

sonic and Alfvénic critical point positions (see Sittler & Guhathakurta (1999))

sonic point and slow solar wind origin (Sheeley et al. 1997) approaching these regions, acceleration plays a role

Wang et al. (2000), sources of slow solar wind + IMF regulation mechanism + blobs; compare with our slow V lognormal part; Parker solution

-> below $20 R_s$ PSP will fly well into sw acceleration region

Sheeley et al. (1997) -> LASCO coronagraph observed speed profile of coronal features tracing the slow solar wind, $2\text{--}30 R_s$

- sonic point $5\text{--}6 R_s$

- slow solar wind origin $3\text{--}4 R_s$

The near-Sun (PSP perihelion) solar wind velocity is expected to be slower than our model's estimates, because the position of the source (Alfvénic critical) surface is predicted to lie between $15\text{--}30 R_s$ (Schatten1969, Sittler1999, Exarhos2000, Katsikas2010, Goelzer2014; choose references...), up to which the solar wind is believed to be accelerated.

The Parker (1958) model of an isothermal expanding corona with a temperature of 10^6 K and a critical radius of $5.8 R_s$.

We expect that even our Sun-nearest extrapolated density at PSP perihelion agrees well with the actual, since Leblanc et al. (1998) derived an electron density model from type III radio burst observations. Their model shows that the density distance dependency scales with r^{-2} and steepens not until below $10 R_s$ with r^{-6} (see Fig. 11).

magnetic field and temperature:
crossing distance effect

7.3. PSP solar wind environment estimation

Implementing the orbital distance data and predicted SSN for the mission time we can derive PSP's estimated solar wind environment $W'''(x, ssn, r)$.

⁵ <http://sidc.be/silso/forecasts>

⁶ <http://www.swpc.noaa.gov/products/solar-cycle-progression>

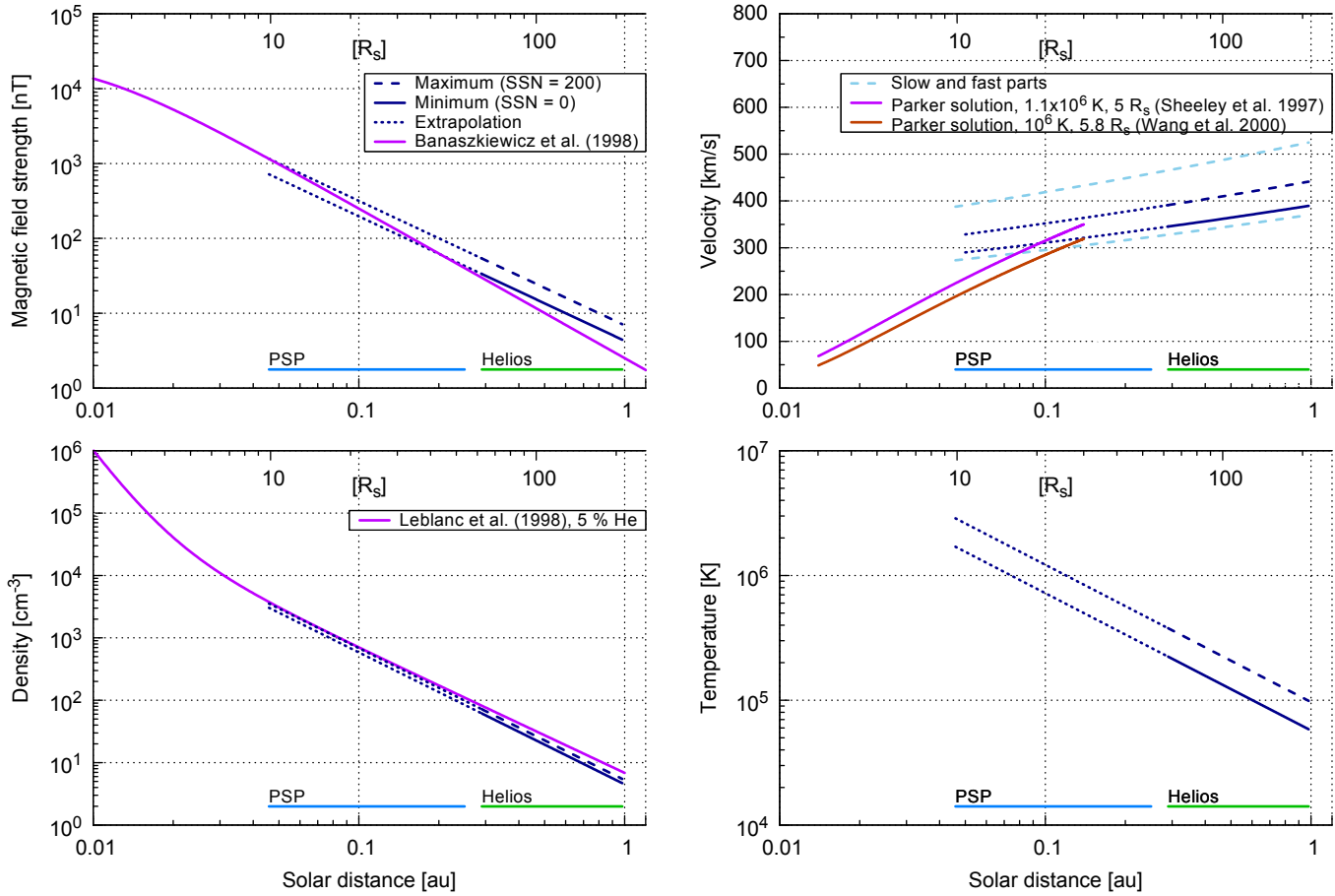


Fig. 11. Radial extrapolation of the solar wind parameters to the PSP orbit region. The from Helios and OMNI measurements obtained models are extrapolated to the PSP region—for the extreme cases of solar minimum (SSN = 0) and maximum (SSN = 200). Note that there is a time lag to the SSN depending on the solar wind parameter. The magnetic field radial dependence is slightly flatter than the analytic DQCS model for solar minimum which Banaszkiewicz et al. (1998) derived. Below $20 R_s$ the slow wind velocity is overestimated in comparison to the measurements from Wang et al. (2000) and (Sheeley et al. 1997). They derived temperature and sonic point values for slow solar wind with the isothermal expansion model (Parker 1958). Down to PSP's perihelion the density is in good agreement with the model from Leblanc et al. (1998). to 1-column...?

The zoom into the first and the nearest perihelia show which solar wind parameter magnitudes can be expected there (Figs. 12 and 13).

7.4. Model validity and error sources

validity and estimation of error size outside of valid model range...

derive heliocentric distance depending error...

list simplifications/approximations...

error estimation for general model and extreme value tendencies

error sources:

- extrapolation
- lognormal model
- SSN variance

all estimates outside these boundaries are extrapolations with large uncertainties.

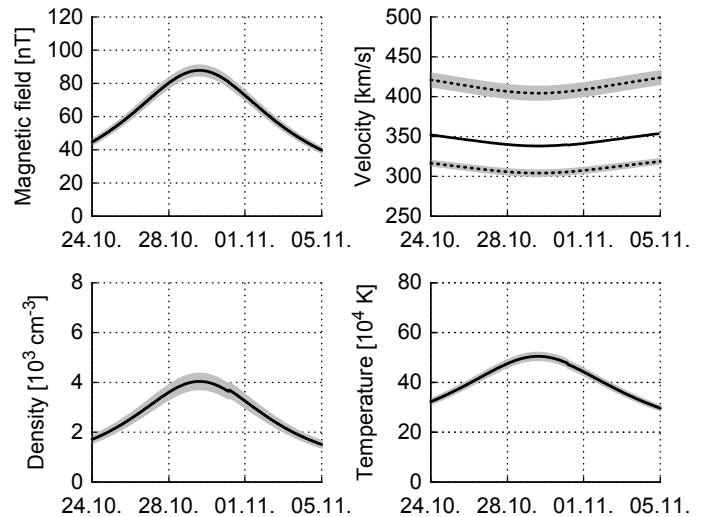


Fig. 12. Estimated solar wind parameter medians (black) and their error bands (grey) during 12 days in 2018 with PSP's first perihelion at about 0.16 au. For the velocity the combined median is calculated and also the SSN independent slow and fast parts are plotted (dotted).

discuss high value zoom figures

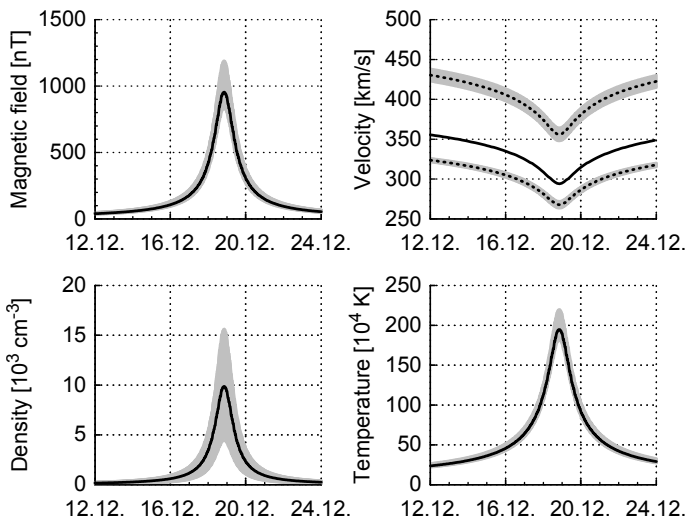


Fig. 13. Estimated solar wind parameter medians (black) and their error bands (grey) during 12 days in 2024 with PSP's nearest perihelion at 0.0459 au. For the velocity the combined median is calculated and also the SSN independent slow and fast parts are plotted (dotted).

The solar wind parameters vary with solar distance as well as with latitudinal separation from the heliospheric current sheet (HCS).

The OMNI data is time-shifted to the nose of the Earth's bow shock. This leads to yearly solar distance variations of > 2 % (cite?) as the Earth orbits the Sun. Furthermore, its orbit within the ecliptic leads to a yearly variation of $\pm 7.2^\circ$ in heliospheric latitude.

The HCS's position in latitude is highly variable around the solar equator (Schwenn 1990, p. 127 ff?).

Error estimation over the year (seasonal/monthly) -> we expect variations to be less than 5 %

8. Results and discussion

list of results:

- empirical solar wind model for inner heliosphere within ecliptic
- low velocity at 0.0459 au
- slow/fast ratio SSN dependency
- application validity of lognormal distributions
- > B inversion of frequency distribution
- > magnetic field distribution's with distance increasing high value tail -> source are compression regions (why with density no increase?); look into Parker1958's B-field formula...
- varying shape with distance is indicator for internal physical processes (mixing/turbulence...)

Balogh et al. (1999) p. 162 ff (origin and formation of CIRs in inner heliosphere with Helios data; latitude V dependence)
Balogh2009 (HMF review + inner heliosheath)
Aschwanden2004, p. 29

individual velocity part discussion -> there is no specific velocity threshold between slow and fast solar wind types, the velocity ranges of both types overlap.

Not only the slowest wind but also the fastest wind is expected to converge to the average speed (Sanchez-Diaz2016 p. 2835,

using MHD-model -> very slow solar wind is continuation of slow wind) (because of interaction).

The ratio of both varies with solar activity, e.g. 3 years after maximum, polar coronal holes are observed to often have equatorial extensions (cite?). see and use Bougeret et al. (1984) p. 498...

larger influx from higher latitudes (see figure b))

In most studies the density distance dependence is assumed to scale with r^{-2} (cites), assuming a constant velocity.

9. Conclusions

Further investigations should be done into structure extrapolations; outward extension of model to Mars seems feasable...

Further questions:

nearer to the Sun (at and below the source surface) the solar wind expansion in the ecliptic should be less spherical but more circular due to the influx from higher latitudes. => density exponent > -2
see Li2011 Fig. 1

Acknowledgements. This work was done within the scope of the Coronagraphic German and US SolarProbePlus Survey (CGAUSS), funded by the German Aerospace Center (DLR) (grant number...).

The authors thank the Helios and OMNI PIs/teams for creating and making available the solar wind in situ data. The Helios and the OMNI data are supplied by the NASA Space Science Data Coordinated Archive (NSSDCA) and the Space Physics Data Facility (SPDF) at NASA's Goddard Space Flight Center (GSFC).

Additional thanks for maintaining and providing the international sunspot number series goes to the World Data Center – Sunspot Index and Long-term Solar Observations (WDC-SILSO) at the Solar Influences Data Analysis Center (SIDC), Royal Observatory of Belgium (ROB).

The PSP SPICE kernel was kindly provided by Angelos Vourlidas (check...).

References

- Balogh, A., Bothmer, V., Crooker, N. U., et al. 1999, Space Sci. Rev., 89, 141
- Banaszkiewicz, M., Axford, W. I., & McKenzie, J. F. 1998, A&A, 337, 940
- Biermann, L. 1951, ZAp, 29, 274
- Bougeret, J.-L., King, J. H., & Schwenn, R. 1984, Sol. Phys., 90, 401
- Feldman, W. C., Asbridge, J. R., Bame, S. J., & Gosling, J. T. 1978, J. Geophys. Res., 83, 2177
- Fox, N. J., Velli, M. C., Bale, S. D., et al. 2015, Space Sci. Rev.
- Gurnett, D. A., Kurth, W. S., Burlaga, L. F., & Ness, N. E. 2013, Science, 341, 1489
- Kasper, J. C., Stevens, M. L., Korreck, K. E., et al. 2012, ApJ, 745, 162
- King, J. H. & Papitashvili, N. E. 2005, Journal of Geophysical Research (Space Physics), 110, A02104
- Leblanc, Y., Dulk, G. A., & Bougeret, J.-L. 1998, Sol. Phys., 183, 165
- McGregor, S. L., Hughes, W. J., Arge, C. N., Odstrcil, D., & Schwadron, N. A. 2011a, Journal of Geophysical Research (Space Physics), 116, A03106
- McGregor, S. L., Hughes, W. J., Arge, C. N., Owens, M. J., & Odstrcil, D. 2011b, Journal of Geophysical Research (Space Physics), 116, A03101
- Neugebauer, M. & Snyder, C. W. 1966, J. Geophys. Res., 71, 4469
- Parker, E. N. 1958, ApJ, 128, 664
- Richardson, I. G. & Cane, H. V. 2012, Journal of Space Weather and Space Climate, 2, A2
- Rosenbauer, H., Schwenn, R., Marsch, E., et al. 1977, Journal of Geophysics Zeitschrift Geophysik, 42, 561
- Schwenn, R. 1983, in NASA Conference Publication, Vol. 228, NASA Conference Publication
- Schwenn, R. 1990, Large-Scale Structure of the Interplanetary Medium, ed. R. Schwenn & E. Marsch, 99

- Sheeley, N. R., Wang, Y.-M., Hawley, S. H., et al. 1997, ApJ, 484, 472
SILSO World Data Center. 1963–2016, International Sunspot Number Monthly
Bulletin and online catalogue
Sittler, Jr., E. C. & Guhathakurta, M. 1999, ApJ, 523, 812
Smith, E. J. & Balogh, A. 2003, in American Institute of Physics Conference Series, Vol. 679, Solar Wind Ten, ed. M. Velli, R. Bruno, F. Malara, & B. Bucci, 67–70
Vourlidas, A., Howard, R. A., Plunkett, S. P., et al. 2016, Space Sci. Rev., 204, 83
Wang, Y.-M., Sheeley, N. R., Socker, D. G., Howard, R. A., & Rich, N. B. 2000, J. Geophys. Res., 105, 25133